Theory and measurements of convective Raman side scatter in inertial confinement fusion experiments

P. Michel,[1] M. J. Rosenberg,[2] W. Seka,[2] A. A. Solodov,[2] R. W. Short,[2] T. Chapman,[1] C. Goyon,[1] N. Lemos,[1] M. Hohenberger,[1] J. D. Moody,[1] S. P. Regan,[2] and J. F. Myatt[2,*]

[1]*Lawrence Livermore National Laboratory, Livermore, CA 94551, USA*

[2]*Laboratory for Laser Energetics, University of Rochester, Rochester, New York, NY 14623-1299, USA*

(Received 15 June 2018; revised manuscript received 4 January 2019; published 13 March 2019)

Raman side scatter, whereby scattered light is resonant while propagating perpendicularly to a density gradient in a plasma, was identified experimentally in planar-target experiments at the National Ignition Facility at intensities orders of magnitudes below the threshold for absolute instability. We have derived a new theoretical description of convective Raman side scatter below the absolute threshold, validated by numerical simulations. We show that inertial confinement fusion experiments at full ignition scale, i.e., with mm-scale spot sizes and density scale lengths, are prone to increased coupling losses from Raman side scatter as the instability can extend from the absolute regime near the quarter-critical density to the convective regime at lower electron densities.

DOI: 10.1103/PhysRevE.99.033203

I. INTRODUCTION

Inertial confinement fusion (ICF) [1] experiments aim to implode and compress deuterium-tritium fuel capsules to thermonuclear ignition and burn using lasers. The capsules are imploded via the rocket effect of the blow-off of an ablator outer layer on the capsule [2,3]; the ablator can be driven either directly by lasers in the "direct-drive" (DD) scheme [4] or indirectly via the x rays from the interior walls of a "hohlraum" cavity surrounding the capsule and irradiated by lasers in the "indirect-drive" geometry [5]. In either configuration, electron plasma waves (EPW) can be resonantly driven by laser-plasma instabilities (LPI). These EPWs can trap and accelerate electrons to suprathermal energies, which can prematurely preheat the fuel and impede compression and can scatter the laser away from the target, reducing the laser energy coupling. The main LPI processes coupling laser light and EPWs are stimulated Raman scattering (SRS) and two-plasmon decay (TPD) [6].

One particular SRS geometry which received great attention in the 1970s is tangential side scatter, whereby the scattered light is resonant at its "turning point" in a density gradient, i.e., where it propagates perpendicularly to the gradient, following a constant density contour [7–10]. This process constitutes the only situation where SRS can become "absolute" (i.e., exponentially growing in time at a fixed spatial location, rapidly reaching saturation via pump depletion or other nonlinear processes) in low-density regions below $n_c/4$, the quarter-critical density for the laser wavelength; Raman side scatter was therefore initially anticipated to be particularly threatening for ICF, but its observation has remained rather elusive in experiments and thus generated less interest after the 1980s. However, this process has recently been the subject of renewed investigations and interest in the ICF and laser-plasma communities: It was indeed suggested as the generating mechanism for the observation of suprathermal electron "beaming" in indirect-drive ICF experiments (as a collective process via a shared EPW) [11,12] and was also identified in experiments using foam targets at the Omega facility (also as a collective process, via a shared scattered light wave) [13]. However, the laser intensities in most of these experiments were in fact orders of magnitude below the absolute instability threshold for side scatter if the EPW damping is accounted for. The "Rosenbluth gain formula" [14] was used to explain the presence of Raman side scatter in these experiments, since the convective gain value it provides goes to infinity at the turning point; however, this is also incorrect, since that formula ignores the refraction of the scattered light toward lower-density regions, which will keep the convective gain finite. A theoretical justification for these recent observations of side scatter is still lacking.

In this article, we present measurements of Raman side scatter over a wide range of electron densities, from $n_c/4$, where the observation is consistent with an absolute instability, to lower densities (down to $0.1n_c$), where the laser intensity is many orders of magnitude below the absolute threshold. In order to correctly describe the process below the absolute threshold, we have derived a new analytical description of Raman side scatter in the convective regime. This description extends the validity of the "Rosenbluth gain" to the scattered light's turning point by accounting for the refraction of the scattered light which keeps the propagation distance at the resonant density (and thus the amplification gain) finite. This result was validated against numerical integration of the SRS fluid equations in Fourier space. We find that ICF experiments at full scale (∼MJ-laser energies, ∼mm-scale density gradients and laser spots) are more prone to coupling losses from Raman side scatter, as the instability is no longer restricted to the absolute regime near the quarter-critical density but can extend to lower densities by having sufficient

*Present address: Department of Electrical and Computer Engineering, University of Alberta, Edmonton, AB T6G 1H9, Canada.

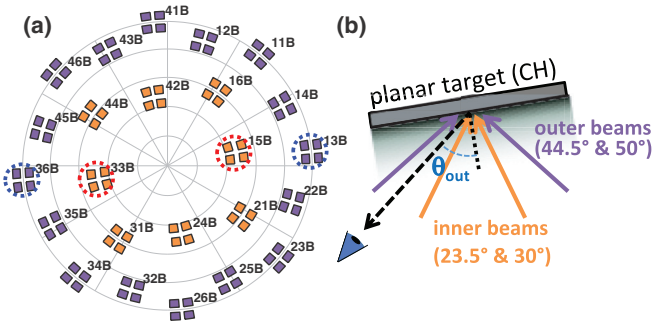

FIG. 1. (a) Polar view (Lambert azimuthal projection) of the NIF's 96 southern hemisphere beams. (b) Target alignment and geometry; a tilt was used to vary the angle θ_{out} between the target surface and the FABS diagnostics (located in the quads 36B and 31B).

gain and amplification length in the convective regime. The new methodology and findings from this paper were recently applied to interpret an experimental investigation of suprathermal electron generation in ICF [15], where it was shown that tangential side scatter is a major contributor to the generation of suprathermal electrons in full-scale DD conditions.

II. EXPERIMENTS

The experiments described in this article were conducted using the southern hemisphere of the National Ignition Facility (NIF) laser (96 beams, i.e., 24 quadruplets or "quads" grouped into "outer cones" at 44.5° and 50° from the vertical axis and "inner cones" at 23.5° and 30°). The target was a planar thick CH slab, with a variable tilt from horizontal introduced to scan the collection angle θ_{out} of the scattered light into the full aperture backscatter station (FABS) diagnostics (at fixed locations in the target chamber [16]) from the target normal (Fig. 1). Three-dimensional (3D) simulations using the code Hydra [17] were performed to verify that the expansion of the plasma remains mostly 1D up to tilt angles of ∼30°. Every quad had the same peak intensity, 2.2×10^{14} W/cm^2. These experiments were designed to produce laser and plasma conditions relevant to full-scale direct-drive ICF conditions at reduced total laser energy [15], producing a roughly 1D plasma expansion due to the large spot sizes (∼1–2 mm) of the NIF laser [18].

For a 1D density profile along z, the expected exit angle of the Raman-scattered light θ_{out} is easily derived for a given SRS wavelength λ_s using refraction laws for the SRS and laser light waves. Defining ω_0, $\boldsymbol{k}_0(z)$ [respectively, ω_s, $\boldsymbol{k}_s(z)$] as the laser's (respectively, scattered light wave's) frequency and wave number and $\omega_{pr} = \omega_{pe}(z = z_r)$ the resonant electron plasma frequency such that $\omega_b^2 = \omega_{pr}^2 + 3k_b^2 v_e^2$ (where $v_e = \sqrt{T_e/m_e}$ is the electron thermal velocity and $\omega_b = \omega_0 - \omega_s$, $\boldsymbol{k}_b = \boldsymbol{k}_0 - \boldsymbol{k}_s$ are the frequency and wave number of the laser and scattered light's beat wave), we get:

$$\sin(\theta_{\text{out}}) = \begin{cases} \sin(\theta_0)\sqrt{\frac{1-\omega_{pr}^2/\omega_s^2}{1-\omega_{pr}^2/\omega_0^2}} & \text{(backscatter)} \\ \sqrt{1-\omega_{pr}^2/\omega_s^2} & \text{(side scatter)} \end{cases}, \quad (1)$$

where θ_0 is the laser incidence angle in vacuum. For backscatter, the SRS exit angle is always smaller than θ_0 and approaches 0 when $n_e(z_r) \to n_c/4$. Whereas for side scatter, it can take any value in $[0, \pi/2]$ depending almost exclusively on λ_s, with only a weak dependence on θ_0 and the electron temperature (the only dependence of θ_{out} on the laser incidence angle is via k_b in the Bohm-Gross relation and is typically negligible). The measurement of θ_{out} vs. λ_s should thus provide a clear signature of side scatter and in particular help clearly distinguish it from backscatter.

Figure 2(a) shows the expected exit angle θ_{out} for side scatter as a function of wavelength for two electron temperatures $T_e = 3$ and 5 keV, bracketing the ∼4 keV ± 20% measured in the experiments; these measurements were performed via dot spectroscopy and by looking at the spectral shift of the $\omega_0/2$ feature and were consistent with rad-hydro simulations [15]. This plot also shows experimental measurements of the Raman-scattered light wavelength at four collection angles $\theta_{\text{out}} = [59°, 50°, 30°, 0°]$. The observed wavelengths show an excellent agreement with the theoretical expectation for side scatter; the electron densities corresponding to the measured collection angles range from 0.1 to $0.25n_c$.

In particular, Fig. 2(c) shows the time- and spectrally resolved SRS measurements at 50° (note that the amplitude modulation at 3 GHz in the SRS signal corresponds to frequency to amplitude modulation modulation in the laser, nonlinearly amplified by SRS). For this experiment, the outer and inner cones of beams were shot one after the other, as shown in Fig. 2(b); the target was horizontal in the target chamber (no tilt). The wavelength of the SRS signal stayed unchanged regardless of the incidence angle of the lasers, which is another distinctive signature of side scatter [Eq. (1)]. Note that in addition to the narrow-band signal at $2\lambda_0$, the normal incidence measurement also had a broad feature at ∼600 nm, as seen in Ref. [15], whose origin is still unexplained.

Next, we repeated the experiment at the 50° collection angle [Figs. 2(b) and 2(c)] but with selected quads turned off in order to help identify the origins of the SRS observed in Q36B FABS; indeed, since the side-scatter exit angle is essentially independent of the laser incidence, any one (or multiple) beam(s) can potentially drive the observed SRS. The results are shown in Fig. 2(d), where four quads [36B, 13B, 15B, and 33B, highlighted in Fig. 1(a)] were successively turned off. The SRS dropped significantly when Q36B and Q33B were turned off, by ∼95% and ∼50%, respectively, whereas turning off the opposed quad had comparatively little effect. This indicates that most of the measured SRS signal at 50° is a single-quad process, driven by the quad in the most opposite direction to the SRS which maximizes the side-scatter gain (as shown below). While recent work (Refs. [11,13]) brought attention to collective processes for Raman side scatter (where multiple lasers collectively drive a shared EPW or scattered light wave), these observations show that the instability can also exist as a single-quad process.

III. THEORY

The well-known "Rosenbluth gain" formula [14] is often used to evaluate the risk of LPI processes such as SRS or TPD in a nonuniform plasma; however, it is invalid near the turning

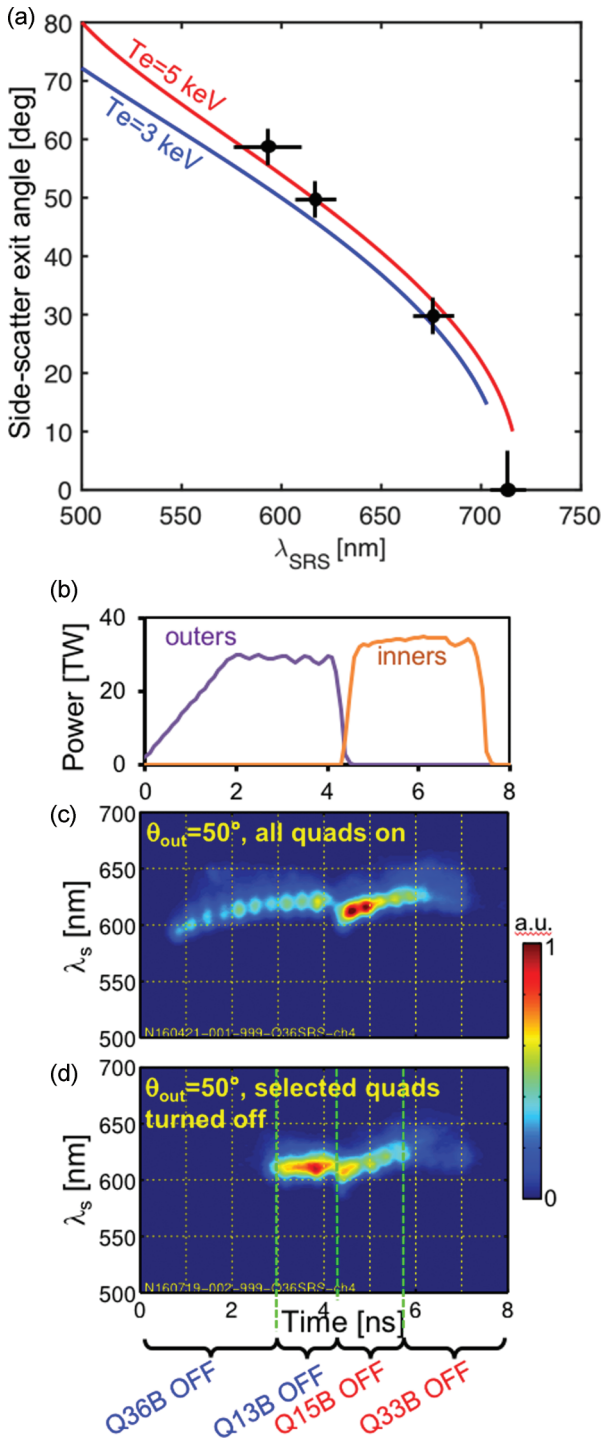

FIG. 2. (a) Expected exit angle for Raman side scatter [Eq. (1)] for two electron temperatures, $T_e = 3$ and 5 keV (bracketing the ~4 keV estimated temperature in the experiments), and FABS measurements at four collection angles $\theta_{\text{out}} = [59°, 50°, 30°, 0°]$. (b) Laser pulse shape for collection at $\theta_{\text{out}} = 50°$ (in this case the target was horizontal and the data were collected in FABS 36B). (c) SRS spectrum from the 50° collection angle with all quads turned on, showing the same observed wavelength wether the outer cones (44.5° and 50° incidence) or inner cones (23.5° and 30°) were shot. (d) Same as (c) with selected quads turned off as indicated [the selected quads are highlighted in Fig. 1(a)].

point of the scattered light, as it ignores refraction which will keep the propagation length through the resonance region (and thus the gain) finite and makes use of an envelope or Wentzel–Kramers–Brillouin (WKB) assumption for the scattered light, which breaks down at the turning point. In the following we derive an expression for the gain at the turning point, valid below the absolute instability threshold. We still use a WKB model for the scattered light, which will be justified later.

Developing the fluid response for the density perturbation, $(\partial_t^2 + \omega_p^2 + 2\nu\partial_t - 3v_e^2\nabla^2)\delta n = c^2 n_0 \nabla^2(a_0 a_s)$, where $\nu = \nu_L + \nu_{ei}\omega_b^2/\omega_{pe}^2$ is the EPW damping (sum of the Landau and collisional dampings) and a_0, a_s the laser and scattered light's potential vectors normalized to $e/m_e c^2$ [such that $a_0 \simeq 0.85 \times 10^{-9}\sqrt{I\ (\text{W/cm}^2)}\lambda_0\ (\mu\text{m}^2)$], we get, assuming a forced response of the plasma to the beat wave and an un-depleted laser: $\delta n = \frac{1}{2}k_b^2 n_0 c^2 a_0 a_s^*/(D + 2i\nu\omega_b)$, where $D(\boldsymbol{k}_b, \omega_b) = \omega_b^2 - \omega_p(z)^2 - 3k_b(z)^2 v_e^2$ (with $D = 0$ at $z = z_r$). The steady-state energy gain exponent G for the SRS light can then be derived starting from the light wave equation, giving:

$$G = \int_S \frac{k_b^2 |a_0|^2 \omega_p^2}{4k_s} \frac{2\nu\omega_b}{D^2 + 4\nu^2\omega_b^2} ds, \tag{2}$$

where the path integral is taken along the propagation of the SRS light.

Away from the turning point, the integration contour S can be approximated as a straight line, with $s = -z/\cos(\theta)$ [cf. Fig. 3(a)]. We define $s = 0$ as the location of the SRS resonance [i.e., $D(0) = 0$, with $D(s) = \omega_b^2 - \omega_{pe}^2(s) - 3v_e^2 k_b^2(s)$], and Taylor-expand $D(s)$ around 0, $D(s) \simeq s\partial_s D(0)$. We get $\partial_s D(0) = \omega_{pr}^2 \cos(\theta)/L$, and the integrand in Eq. (2) takes the usual form of a Lorentzian, giving the following integrated gain (which does not depend on the damping anymore):

$$G = \frac{\pi k_b^2}{4k_s} \frac{a_0^2 L}{\cos(\theta)}. \tag{3}$$

By comparison, the Rosenbluth gain derivation considers three coupled plasma modes (two EM and one EPW) in a density gradient, satisfying $\omega_0 = \omega_s - \omega_L$ (where ω_L is the Langmuir wave frequency) and a wave-vector dephasing $\kappa(z) = k_0(z) - k_s(z) - k_L(z)$; in the vicinity of the resonant density where $\kappa = 0$, the Rosenbluth gain is given by $G_R = 2\pi\gamma^2/[\kappa' v_{sz} v_{Lz}]$, where v_{sz} and v_{Lz} are the group velocities of the scattered light and EPW along z, respectively; $\gamma = k_L c\omega_{pe} a_0/4\sqrt{\omega_0\omega_s}$ is the SRS temporal growth rate; and the prime denotes the derivative along z. Noting that $\kappa' v_{Lz} \simeq \omega_{pr}/2L$, we can easily verify that the "strong damping" gain derivation from Eq. (2) to Eq. (3) recovers the Rosenbluth gain formula.

The size of the resonance region can be estimated by setting $D = \pm 2\nu\omega_b$ (FWHM of the Lorentzian), which gives $\Delta z = 4\nu L/\omega_{pr}$. The $\cos(\theta)$ dependence is not explicit due to the definition of L, taken as the derivative along z not s; taken along s, the length of the resonance is thus $\Delta l = 4\nu L/[\omega_{pr}\cos(\theta)]$ [cf. Fig. 3(a)].

Near the turning point, the ray-tracing equations ($\dot{\boldsymbol{r}} = \boldsymbol{v}_g$, $\dot{\boldsymbol{v}}_g = \frac{1}{2}c^2\nabla\omega_p^2/\omega^2$, where the dot denotes the time derivative) give a parabolic trajectory for the SRS light: $x(t) \simeq v_s t$

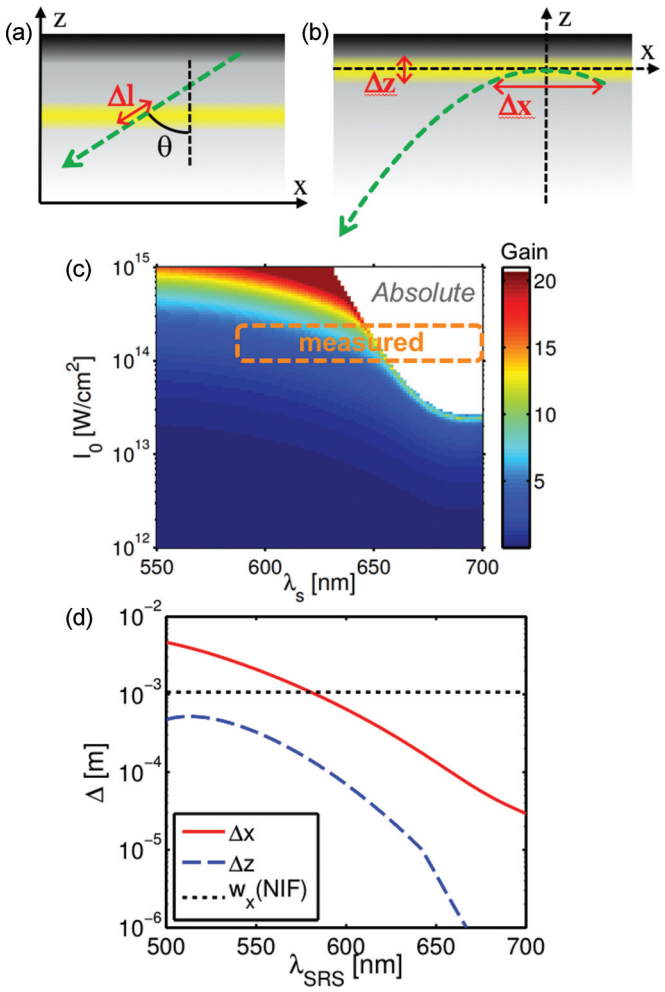

FIG. 3. (a) SRS resonance away from the turning point, as given by the Rosenbluth formula when refraction can be neglected (1D problem); the length of the resonance region is approximately Δl along the path of the scattered light. (b) Tangential side-scatter geometry, where the resonance occurs at the turning point; refraction moves the scattered light away from the resonance and leads to a finite convective gain G and resonance region, defined by Δz and Δx. (c) Side-scatter gain [numerical solution from Eqs. (6) and (7)] vs. wavelength and laser intensity for $L = 800$ μm, $T_e = 4$ keV and $\theta_{0v} = 50°$; the region of absolute instability is marked in white, and the orange region corresponds to our experimental observations (with intensities ranging from 2.2 to 1×10^{14} W/cm^2 to account for the ~50% laser absorption at higher densities). (d) Size of the resonance region Δx and Δz [Eqs. (8) and (9)], and size of the NIF beams projected along the x direction (dotted line).

and $z(t) \simeq -c^2\omega_{pr}^2 t^2/(4L^2\omega_s^2)$ [as illustrated in Fig. 3(b)]. The gain integral can be parametrized with respect to time; here we set $t = 0$ as the time when the scattered light goes through resonance, i.e., $D(t = 0) = 0$. D needs to be expanded to the second order: $D(t) \simeq t\dot{D}(0) + t^2\ddot{D}/2$, with $\dot{D}(0) = -3v_e^2\omega_{pr}^2 k_{0z}/(L\omega_s)$ [where $k_{0z} = \boldsymbol{k}_0(z_r)\cdot\boldsymbol{z}$] and $\ddot{D}(0) = \omega_{pr}^4 c^2/(2L^2\omega_s^2)$. The first-order term comes from the increase in k_b near the turning point (due to the rotation of $\boldsymbol{k}_s$—as was noticed in Ref. [7]), whereas the second-order term comes from the decrease in density as the light moves away from its turning point. In the limit of negligible EPW damping, the SRS lights first moves out of resonance due to the increase of k_b^2 (since $\dot{k}_b^2 \propto t$), which increases $\omega_L^2(t) = \omega_{pe}^2(t) + 3k_b^2(t)v_e^2$ away from ω_b^2; later, the decrease in $\omega_{pe}^2(t)$ ($\propto t^2$) catches up and brings ω_L down, back to ω_b at $t_1 = -2\dot{D}(0)/\ddot{D}(0)$ when $D(t_1) = 0$. In other words, the scattered light is in fact resonant twice, first at the turning point and a second time slightly away from it. The resulting gain, obtained from integrating Eq. (2), is

$$G = 2G_R(0)\frac{k_s c^2}{3v_e^2 k_{0z}}, \tag{4}$$

where $G_R(0)$ is the SRS Rosenbluth gain for normal incidence. However, with EPW damping levels more typical of ICF conditions, the two resonances can overlap and merge, and the quadratic term in the expansion of D ($\propto t^2$) dominates. The gain then takes the following form, explicitly depending on the EPW damping:

$$G = G_R(0)\sqrt{\frac{\omega_s^2 - \omega_{pr}^2}{\omega_{pr}^2}}\sqrt{\frac{\omega_{pr}}{\nu}}, \tag{5}$$

where the damping is evaluated at the turning point.

This expression, which assumes a parabolic trajectory of a wave packet through a linear density gradient, should in principle be equivalent to a straight propagation through a parabolic density profile (with the peak of the spatial gain rate located at the vertex of the parabola in either case); the latter situation was studied in Ref. [19], and one can easily verify that their gain formula is indeed equivalent to ours.

To verify the validity of this expression, we Fourier transform the fluid equations for the EPW and scattered light wave's wave equations with respect to z; this technique avoids using an envelope along z (i.e., using the WKB approximation), which would break down at the turning point of the scattered light. The coupled equations are as follows:

$$\frac{da_s(k)}{dk} = -i\frac{L}{\omega_{pr}^2}D_t a_s(k) + i\frac{L}{2}a_0\eta, \tag{6}$$

$$\frac{d\eta(k)}{dk} = -i\frac{L}{\omega_{pr}^2}D_l\eta(k) + i\frac{Lk_b^2c^2}{2\omega_{pr}^2}a_0^* a_s(k), \tag{7}$$

where $\eta(k) = \delta n^*(k - k_{0z})/n_0$, $D_t = \omega_s^2 - (\omega_{pr}^2 + k_s^2c^2)$, and $D_l = \omega_b^2 - (\omega_{pr}^2 + 3k_b^2v_e^2 + 2i\nu\omega_b)$. Recasting these two equations into a single Schrödinger equation and finding its eigenvalues is a well-known technique to derive analytical solutions for the absolute threshold of TPD and SRS [10,20–22]. Here we follow the technique used by Short *et al.* for TPD [23] and perform a numerical integration of the ODE's, which allows us to recover the analytical results from Ref. [10] for the absolute threshold but also to describe the convective regime of the instability—while including the effects of EPW damping. The numerical integration is performed between the input and output vacuum-plasma boundaries for the scattered light, where the Fourier variable must coincide with the vacuum k vector, i.e., $k = -k_{\text{out}} = \sqrt{(\omega_s/c)^2 - k_{sx}^2}$. The boundary conditions taken at k_{out} ("output" for the scattered light wave but "input" for η, per its definition above) are $a_s(k_{\text{out}}) = 1$, $\eta(k_{\text{out}}) = 0$; the integration is performed from $k = k_{\text{out}}$

to $k = k$ and the convective gain is then simply given by $G = \log(|a_s(k_{\rm out})|^2/|a_s(k)|^2)$—the absolute instability manifests itself by a divergent gain. We have verified that the numerical integration gives very similar results to Eq. (5) when the instability is below its absolute threshold, which will be justified below when analyzing the size of the resonance region.

The gain as a function of laser intensity and scattered light wavelength, together with the absolute threshold boundary, are plotted in Fig. 3(c) for the parameters from the NIF experiments ($L = 800$ μm, $\theta_0 = 50^\circ$, polarization smoothing included by assuming that the p-polarized laser wave drives the same EPW as the s-polarized component but with a lower coupling due to the angle between the two light waves' electric fields). This shows that the observed side-scatter signals for the lower densities are largely below the absolute threshold. Likewise, a similar calculation of the absolute threshold including EPW damping for the conditions of Ref. [13] shows that the single-quad intensity in these experiments was also several orders of magnitude below the absolute threshold. This is due to the EPW damping for typical ICF conditions which pushes the absolute instability threshold (as derived in Ref. [10]) to high laser intensities for densities below ~650 nm. The SRS side-scatter signals observed in our experiments as well as those from Refs. [13] should rather be interpreted using a convective gain expression like the one we derived.

The physical size of the resonance region for tangential side scatter, as illustrated in Fig. 3(b), is

$$\Delta z = 2L\frac{\nu}{\omega_{pr}}, \tag{8}$$

$$\Delta x = 4L\sqrt{\frac{2\nu}{\omega_{pr}}}\sqrt{\frac{\omega_s^2-\omega_{pr}^2}{\omega_{pr}^2}}. \tag{9}$$

This shows that side scatter is unlikely to remain significant for wavelengths below ~600 nm, not only because the gain becomes too small but also because the amplification length along x becomes larger than the size of the laser beams, meaning that the scattered light would leave the laser beam envelope before reaching full amplification. This also explains why our gain formula, based on WKB, gives similar results to the numerical integration of Eqs. (7): Indeed, the WKB solution for a light wave's electric field in a density gradient is highly accurate up to a very narrow region at the turning point (the "Airy depth," where an Airy function is required to correctly describe the electric field's transition to an evanescent mode past the turning point), of order $[L\lambda_s^2/(4\pi^2)]^{1/3} \simeq 2$ μm [6]. Figure 3(d) shows that Δz, the width of the resonance region along z, is typically much larger than the Airy depth, except for wavelengths above 650 nm where the instability is absolute anyway: The convective gain formula is thus appropriate as long as one remains below the absolute threshold, as most of the amplification occurs in a region where WKB remains valid.

At higher wavelengths, the absolute instability might locally deplete the laser, though the measured SRS might not directly reveal this activity due to the strong reabsorption (the narrowness of Δz for $\lambda_s > 600$ nm means that the amplification will be very spatially localized, so reabsorption will be significant). For ICF experiments, this means that side scatter at wavelengths near $n_c/4$ may not necessarily represent a significant coupling loss (since the laser light has already been absorbed by the time it reaches $n_c/4$, e.g., by about 50% in our conditions and since the scattered light will be even more strongly reabsorbed) but might still drive large EPWs that can generate suprathermal electrons, which is a potential concern for DD ICF in particular [15]. Whereas at lower wavelengths, the smaller EPW velocity should generate electrons at lower energies, but the coupling loss might become more significant.

We can estimate the extension of these results to spherical density profiles from DD implosions by comparing the curvature of the scattered light at the turning point to that of the (spherical) density profile. In DD implosions, hydrodynamic scaling preserves the ratio ρ_n/L to ~4, where ρ_n is the radius of curvature of the isodensity surface at the electron densities most relevant to Raman side scatter (~15–20%n_c) and L the gradient scale-length at these densities (whether for sub scale experiments at Omega or full scale at NIF [24]). By comparison, the radius of curvature of a side-scattered ray near its turning point (from the parabola equation derived previously) is $\rho_s = 2L(1-\omega_{pr}^2/\omega_s^2)/(\omega_{pr}^2/\omega_s^2)$. The ratio of the scattered light curvature to the density profile curvature is thus $\rho_s/\rho_n \approx \frac{1}{2}(1-\omega_{pr}^2/\omega_s^2)/(\omega_{pr}^2/\omega_s^2)$. For the SRS wavelengths of interest here ($\lambda_s \geqslant 600$ nm), we have $\omega_{pr}^2/\omega_s^2 \geqslant 0.5$ and therefore $\rho_s/\rho_n \leqslant 0.5$. This means that refraction will move the scattered light out of resonance before the curvature from the density profile does, and Raman side-scatter should still be present in spherical DD implosions at levels comparable to those observed in these experiments.

IV. CONCLUSION AND DISCUSSION

In summary, we have demonstrated the presence of Raman side scatter in ICF experiments at full direct-drive ignition scale, over a wide range of electron densities spanning ~0.1–0.25 n_c. The side-scatter process is inconsistent with an absolute instability for lower densities and should rather be treated as a convective instability for which we provide a simple analytical gain estimate, as well as an estimate for the size of the amplification region. While side scatter is likely limited to densities near $n_c/4$ for small-scale experiments, the combination of large density scale lengths, large laser spot sizes, and high electron temperatures (leading to higher EPW damping) can lead to the presence of side scatter at lower densities in the convective regime, as observed in several recent experiments at the NIF.

Regarding the potential impact of Raman side scatter on ICF experiments: First, for indirect drive, with the currently available suite of diagnostics, we have not obtained any measurements pertaining to SRS that require or even suggest the presence of side scatter in low-gas-fill ($\lesssim$0.3 mg/cc) hohlraums. This is based on two experimental observations: (i) All SRS measured on NIF has been consistent with backscatter, with all the energy contained in a cone of divergence angle ~2–3 times larger than that of the incident quad (cf. typical examples in Ref. [16]). No scattered light was observed outside these cones, including from other backscatter diagnostics on cones that did not generate Raman

backscatter (the lower detection threshold is a few joules falling within a beam's aperture, which would correspond to less than $\sim$10 kJ if extrapolated into 4π sr). (ii) Energy conservation from Manley-Rowe relations dictates that any significant laser energy conversion into Raman side scatter should be accompanied by a comparable energy conversion into hot electrons. The apparent absence of hot electrons ($\ll$1% of laser energy) in recent (2015 onward) experiments using low gas-fill hohlraums makes it unlikely that Raman side scatter is energetically significant in this low-gas-fill hohlraum design space.

In contrast, for direct-drive ICF, Raman side scatter has been identified as one of the main mechanisms responsible for the generation of suprathermal electrons in MJ-scale conditions [15]. While the inferred hot electron preheat is in the acceptable range based on estimates from rad-hydro simulations, it is close to significantly affecting the fuel compressibility and, therefore, further study is warranted.

ACKNOWLEDGMENTS

We thank V. Goncharov, L. Divol, and R. L. Berger for fruitful discussions and feedback. This work was performed under the auspices of the U.S. Department of Energy by Lawrence Livermore National Laboratory under Contract No. DE-AC52-07NA27344.

[1] J. Nuckolls and L. Wood, Nature **239**, 139 (1972).
[2] S. Atzeni and J. Meyer-ter Vehn, *The Physics of Inertial Fusion: Beam Plasma Interaction, Hydrodynamics, Hot Dense Matter*, Vol. 125 (Oxford University Press on Demand, Oxford, 2004).
[3] J. Lindl, Phys. Plasmas **2**, 3933 (1995).
[4] R. L. McCrory, D. D. Meyerhofer, R. Betti, R. S. Craxton, J. A. Delettrez, D. H. Edgell, V. Y. Glebov, V. N. Goncharov, D. R. Harding, D. W. Jacobs-Perkins, J. P. Knauer, F. J. Marshall, P. W. McKenty, P. B. Radha, S. P. Regan, T. C. Sangster, W. Seka, R. W. Short, S. Skupsky, V. A. Smalyuk, J. M. Soures, C. Stoeckl, B. Yaakobi, D. Shvarts, J. A. Frenje, C. K. Li, R. D. Petrasso, and F. H. Seguin, Phys. Plasmas **15**, 055503 (2008).
[5] M. Edwards, P. Patel, J. Lindl, L. Atherton, S. Glenzer, S. Haan, J. Kilkenny, O. Landen, E. Moses, A. Nikroo *et al.*, Phys. Plasmas **20**, 070501 (2013).
[6] W. L. Kruer, *The Physics of Laser Plasma Interactions* (Westview Press, Boulder, CO, 2003).
[7] H. H. Klein, W. M. Manheimer, and E. Ott, Phys. Rev. Lett. **31**, 1187 (1973).
[8] C. S. Liu, M. N. Rosenbluth, and R. B. White, Phys. Fluids **17**, 1211 (1974).
[9] M. A. Mostrom and A. N. Kaufman, Phys. Rev. Lett. **42**, 644 (1979).
[10] B. B. Afeyan and E. A. Williams, Phys. Fluids **28**, 3397 (1985).
[11] P. Michel, L. Divol, E. L. Dewald, J. L. Milovich, M. Hohenberger, O. S. Jones, L. B. Hopkins, R. L. Berger, W. L. Kruer, and J. D. Moody, Phys. Rev. Lett. **115**, 055003 (2015).
[12] E. L. Dewald, F. Hartemann, P. Michel, J. Milovich, M. Hohenberger, A. Pak, O. L. Landen, L. Divol, H. F. Robey, O. A. Hurricane, T. Döppner, F. Albert, B. Bachmann, N. B. Meezan, A. J. MacKinnon, D. Callahan, and M. J. Edwards, Phys. Rev. Lett. **116**, 075003 (2016).
[13] S. Depierreux, C. Neuville, C. Baccou, V. Tassin, M. Casanova, P.-E. Masson-Laborde, N. Borisenko, A. Orekhov, A. Colaitis, A. Debayle, G. Duchateau, A. Heron, S. Huller, P. Loiseau, P. Nicolaï, D. Pesme, C. Riconda, G. Tran, R. Bahr, J. Katz, C. Stoeckl, W. Seka, V. Tikhonchuk, and C. Labaune, Phys. Rev. Lett. **117**, 235002 (2016).
[14] M. N. Rosenbluth, Phys. Rev. Lett. **29**, 565 (1972).
[15] M. J. Rosenberg, A. A. Solodov, J. F. Myatt, W. Seka, P. Michel, M. Hohenberger, R. W. Short, R. Epstein, S. P. Regan, E. M. Campbell, T. Chapman, C. Goyon, J. E. Ralph, M. A. Barrios, J. D. Moody, and J. W. Bates, Phys. Rev. Lett. **120**, 055001 (2018).
[16] J. D. Moody, P. Datte, K. Krauter, E. Bond, P. A. Michel, S. H. Glenzer, L. Divol, C. Niemann, L. Suter, N. Meezan, B. J. MacGowan, R. Hibbard, R. London, J. Kilkenny, R. Wallace, J. L. Kline, J. Jackson, K. Knittel, G. Frieders, B. Golick, G. Ross, K. Widmann, J. Jackson, S. Vernon, and T. Clancy, Rev. Sci. Instrum. **81**, 10D921 (2010).
[17] M. M. Marinak, G. D. Kerbel, N. A. Gentile, O. Jones, D. Munro, S. Pollaine, T. R. Dittrich, and S. W. Haan, Phys. Plasmas **8**, 2275 (2001).
[18] A. A. Solodov, M. J. Rosenberg, J. F. Myatt, R. Epstein, S. P. Regan, W. Seka, J. Shaw, M. Hohenberger, J. W. Bates, J. D. Moody, J. E. Ralph, D. P. Turnbull, and M. A. Barrios, J. Phys.: Conf. Ser. **717**, 012053 (2016).
[19] C. Niemann, R. Berger, L. Divol, R. Kirkwood, J. Moody, C. Sorce, and S. Glenzer, JINST **6**, P10008 (2011).
[20] R. White, P. Kaw, D. Pesme, M. Rosenbluth, G. Laval, R. Huff, and R. Varma, Nucl. Fusion **14**, 45 (1974).
[21] C. S. Liu and M. N. Rosenbluth, Phys. Fluids **19**, 967 (1976).
[22] A. Simon, R. W. Short, E. A. Williams, and T. Dewandre, Phys. Fluids **26**, 3107 (1983).
[23] R. W. Short, Bull. Am. Phys. Soc. **55** (2010).
[24] V. N. Goncharov (private communication).